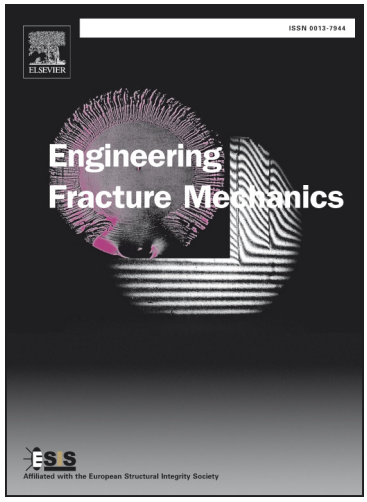

Element-wise fracture algorithm based on rotation of edges

P. Areias, T. Rabczuk, D. Dias-da-Costa

PII: S0013-7944(13)00237-3
DOI: http://dx.doi.org/10.1016/j.engfracmech.2013.06.006
Reference: EFM 4078

To appear in: *Engineering Fracture Mechanics*

Received Date: 13 October 2012
Revised Date: 28 March 2013
Accepted Date: 24 June 2013

Please cite this article as: Areias, P., Rabczuk, T., Dias-da-Costa, D., Element-wise fracture algorithm based on rotation of edges, *Engineering Fracture Mechanics* (2013), doi: http://dx.doi.org/10.1016/j.engfracmech.2013.06.006

Element-wise fracture algorithm based on rotation of edges

P. Areias[ϱ⋆], T. Rabczuk[•,⋆], D. Dias-da-Costa[+◇]

13th July 2013

[ϱ]Physics Department
University of Évora
Colégio Luís António Verney
Rua Romão Ramalho, 59
7002-554 Évora, Portugal

[•]Professor
School of Civil, Environmental and Architectural Engineering
Korea University
[+]INESC Coimbra
Rua Antero de Quental 199, 3000-033 Coimbra
[◇]Civil Eng. Dept., University of Coimbra
Rua Luís Reis Santos
3030-788 Coimbra, Portugal

[⋆]ICIST

Abstract

We propose an alternative, simpler algorithm for FEM-based computational fracture in brittle, quasi-brittle and ductile materials based on edge rotations. Rotation axes are the crack front edges (respectively nodes in surface discretizations) and each rotated edge affects the position of only one or two nodes. Modified positions of the entities minimize the difference between the predicted crack path (which depends on the specific propagation theory in use) and the edge or face orientation. The construction of all many-to-many relations between geometrical entities in a finite element code motivates operations on existing entities retaining most of the relations, in contrast with remeshing (even tip remeshing) and enrichment which alter the structure of the relations and introduce additional entities to the relation graph (in the case of XFEM, enriched elements which can be significantly different than classical FEM elements and still pose challenges for ductile fracture or large amplitude sliding). In this sense, the proposed solution has algorithmic and generality advantages. The propagation algorithm is simpler than the aforementioned alternatives and the approach is independent of the underlying element used for discretization. For history-dependent materials, there are still some transfer of relevant quantities between meshes. However, diffusion of results is more limited than with tip or full remeshing. To illustrate the advantages of our approach, two prototype models are used: tip energy dissipation (LEFM) and cohesive-zone approaches. The Sutton crack path criterion is employed. Traditional fracture benchmarks and newly proposed verification tests are solved. These were found to be very good in terms of crack path and load/deflection accuracy.

Nomenclature

a	Crack closure parameter
$\boldsymbol{b}_\star$	Nominal body force
d	Damage variable for the cohesive law
$\boldsymbol{e}$	External forces
$\hat{\boldsymbol{e}}_I, \hat{\boldsymbol{e}}_{II}, \hat{\boldsymbol{e}}_{III}$	Modes I, II and III opening directions (normalized)
f_t	Normal stress

[⋆]Corresponding Author.

f_I^+,f_{II}^+,f_{III}^+	Internal forces of modes I, II and III
$\boldsymbol{f}_{0i}^+$	Internal force vector at the tip
$\dot{F}$	External force power
$\boldsymbol{i}$	Internal forces
$\boldsymbol{I}$	Identity matrix
J	Strain energy release rate
J_R	LEFM fracture energy
$\boldsymbol{K}$	Stiffness matrix
$\boldsymbol{l}$	Derivative of the constraint equation
$\boldsymbol{n}$	Normal to the plane or the shell surface
$\boldsymbol{p}$	Crack path direction
Q	Load proportionality factor
$\dot{q}$	Velocity proportionality factor
$\boldsymbol{r}$	Residual
s	Area of Γ_{c_a}
s_c	Constraint equation
$\dot{S}$	Cohesive force power
t	Time
$\boldsymbol{t}_\star$	Imposed surface load
$\boldsymbol{t}_u$	Reactive surface vector
$\boldsymbol{t}$	Cohesive traction for the quasi-brittle case
$\boldsymbol{t}_\lambda$	Cohesive traction for the brittle case
T	Total time of analysis
$\boldsymbol{T}_{\text{mode}}$	Transformation matrix at the tip
u_t	Modes II and III equivalent displacement
u_I,u_{II},u_{III}	Displacement components of modes I, II and III
$\boldsymbol{u}$	Displacement vector field
$\boldsymbol{u}_\star$	Imposed displacement
$[[\boldsymbol{u}]]$	Displacement jump
$[[\dot{\boldsymbol{u}}]]$	Virtual velocity jump
$\dot{W}$	Strain power
W_p	Plastic work
$\boldsymbol{x}_0$	Tip coordinates
$\boldsymbol{x}_1, \boldsymbol{x}_2$	Coordinates of the two neighbor (opposing) nodes connected by external edges to the tip
β	Modes II and III parameter
Γ_c	Crack surface in the deformed configuration
Γ_{c_a}	Active crack surface, $\Gamma_{c_a} \subset \Gamma_c$

Δs	Increment of s
$\dot{\boldsymbol{\varepsilon}}$	Strain rate
$\dot{\boldsymbol{\varepsilon}}_p$	Plastic strain rate
θ_c	Crack path angle
κ	Kinematical variable for the cohesive law
κ_0	Initial κ
σ	Normal cohesive stress
$\boldsymbol{\sigma}$	Cauchy stress tensor
τ_{II},τ_{III}	Tangential cohesive stress components for modes II and III
ϕ	Damage loading function
Ω	Body deformed configuration integration domain

1 Introduction

Discretization methods for computational fracture can be performed with meshfree (cf. [55, 54, 52, 53, 64, 65]) and finite elements (cf. [5, 27]). In the former, crack propagation algorithms have been developed in the past two decades with varying degrees of effectiveness and generality. Existing techniques can be classified as discrete or continuum-based (including combinations of these). A non-exhaustive list is:

- Full and localized rezoning and remeshing approaches [21, 30, 9, 14], variants of local displacement [46, 45, 38, 42] (or strain [49, 2]) enrichments, clique overlaps [37], edges repositioning or edge-based fracture with R-adaptivity [44];
- Element erosion [61], smeared band procedures [48, 51], viscous-regularized techniques [35, 56], gradient and non-local continua [59];
- Phase-field models based on decoupled optimization (equilibrium/crack evolution) with sensitivity analysis [25].

For finite strain simulations, each one has particular advantages and shortcomings, most well documented. However, numerical experimentation is the key for obtaining sound conclusions. In particular, the extended finite element method (XFEM) by Moës, Belytschko and co-workers [47, 20, 46, 15, 63, 23, 24] was used previously but still poses challenges for large amplitude displacements (this is particularly critical for quasi-adiabatic shear bands). Densification of the Jacobian matrix occurs due to pile-up of degrees-of-freedom for nodes contributing to multiple cracks. If n_c cracks are present in elements in the support of a given node, this has $(1+n_c)n_{SD}$ degrees of freedom where n_{SD} is the number of original degrees-of-freedom per node; this produces a fill-in in the sparse Jacobian contrasting with remeshing that retains sparsity along the analysis. The tradeoff is between densification and intricacy (produced by enrichment methods) and increased number of degrees-of-freedom (created by remeshing algorithms). However, the adaptation of classical contact and cohesive techniques to deal with enriched elements is somehow redundant. It is worth noting that large amplitude displacements are managed (see, e.g. [41]) by XFEM *if* neither contact nor cohesive forces are present. Many examples exist for XFEM with both contact and cohesive forces ([7, 12]) but the generality of the results is limited by the kinematic assumptions, stricter than with remeshing.

Difficulties in XFEM are often mitigated at the cost of intricate coding. As a consequence of these difficulties, typically simplified examples are displayed. From the enumerated options, it is often pointed out that local remeshing techniques lead to ill-formed elements (in particular blade and dagger-shaped triangles) which compromise the solution accuracy. These ill-formed elements motivate, besides other aspects, the use of full remeshing. Recently, we proposed a new methodology to attenuate this problem (cf. [9]). In the present work, we further simplify the solution by moving edges so that they align with the predicted crack path.

The work is organized as follows: Section 2 presents the principle of virtual power for cracked bodies with cohesive regions, Section 3 shows the virtual crack closure technique for determination of energy release rate, the cohesive discretization and both the initiation and propagation algorithms. Section 4 presents seven examples of fracture where comparisons with experimental results and alternative techniques are made. Finally, Section 5 shows the conclusions.

2 Principle of virtual power for cracked bodies with cohesive regions

Brittle and quasi-brittle fracture are distinguished by the geometry of the regions where energy dissipation occurs: in brittle fracture energy is dissipated in a crack edge or tip and in quasi-brittle fracture energy is dissipated in a surface (typically identified as cohesive surface). We take a direct approach for dealing with equilibrium problems with cracks (both brittle and quasi-brittle). The formulation is based on the following approach:

- Explicitly including external loads and imposed velocities.
- Including the cohesive zone (identified as Γ_c) where the displacement jump is identified as $[[\dot{\boldsymbol{u}}]]$. Note that part or whole of Γ_c may be unknown.
- Using a load parameter Q for proportional loading and a velocity parameter $\dot{q}$ for proportional imposed velocity:

$$\begin{aligned}\int_\Omega \boldsymbol{\sigma} : \dot{\boldsymbol{\varepsilon}} \mathrm{d}\Omega \quad &= \quad \int_\Omega Q\boldsymbol{b}_\star \cdot \dot{\boldsymbol{u}} \mathrm{d}\Omega + \int_{\Gamma_t} Q\boldsymbol{t}_\star \cdot \dot{\boldsymbol{u}} \mathrm{d}\Gamma_t \\ &\quad + \int_{\Gamma_u} \dot{q}\boldsymbol{t}_u \cdot \boldsymbol{u}_\star \mathrm{d}\Gamma_u + \int_{\Gamma_c} \boldsymbol{t}\left([[\boldsymbol{u}]]\right) \cdot [[\dot{\boldsymbol{u}}]] \mathrm{d}\Gamma_c\end{aligned} \tag{1}$$

where $\boldsymbol{\sigma}$ is the Cauchy stress tensor, $\dot{\boldsymbol{\varepsilon}}$ is the strain rate, $\boldsymbol{b}_\star$ is the nominal body force, $\boldsymbol{t}_\star$ is the imposed surface load, $\boldsymbol{t}_u$ is the *reactive* surface traction and $\boldsymbol{t}$ is the cohesive traction. The unknown field is the displacement $\boldsymbol{u}$. $\boldsymbol{u}_\star$ is the nominal imposed displacement. Equation (1) has two interpretations: equivalence between internal and external power and, if the time derivative of displacement is interpreted as the virtual velocity, it is a form of the principle of virtual power with the required $\forall \dot{\boldsymbol{u}}$ in the space of test functions (cf. [4] for the continuum case). The subset of Γ_c where $[[\boldsymbol{u}]] \neq \boldsymbol{0}$ is denoted Γ_{c_a} (the *active* cohesive zone). For strictly closed cracks we have $[[\boldsymbol{u}]] \cdot \boldsymbol{t} = \boldsymbol{0}$ on Γ_c, implying that $\boldsymbol{t}$ is a Lagrange multiplier (we now can use the notation $\boldsymbol{t}_\lambda$) and the equation (1) is adapted to read:

$$\begin{aligned}\underbrace{\int_\Omega \boldsymbol{\sigma} : \dot{\boldsymbol{\varepsilon}} \mathrm{d}\Omega}_{\dot{W}} \quad &= \quad \underbrace{\int_\Omega Q\boldsymbol{b}_\star \cdot \dot{\boldsymbol{u}} \mathrm{d}\Omega + \int_{\Gamma_t} Q\boldsymbol{t}_\star \cdot \dot{\boldsymbol{u}} \mathrm{d}\Gamma_t + \int_{\Gamma_u} \dot{q}\boldsymbol{t} \cdot \boldsymbol{u}_\star \mathrm{d}\Gamma_u}_{\dot{F}} \\ &\quad + \underbrace{\int_{\Gamma_c} \left(\boldsymbol{t}_\lambda \cdot [[\dot{\boldsymbol{u}}]] + \dot{\boldsymbol{t}}_\lambda \cdot [[\boldsymbol{u}]]\right) \mathrm{d}\Gamma_c}_{\dot{S}}\end{aligned} \tag{2}$$

where $\boldsymbol{t}_\lambda$ is now an independent field at the crack faces, the Lagrange multiplier field conjugate to the constraint $[[\boldsymbol{u}]] = \boldsymbol{0}$. A unified treatment of brittle and quasi-brittle fracture results from establishing (1) and (2) as, respectively, the penalized and the Lagrange-multiplier versions of a constrained problem permits . In (2) the energy is released by the increase of size of $\Gamma_{c_a} \subset \Gamma_c$, whereas in (1) energy is released by growth of Γ_{c_a}. We use s for the area of surface Γ_{c_a}. The strain work is calculated as:

$$W = \int_0^T \dot{W} \mathrm{d}t \tag{3}$$

where T is the total time of analysis and t is the time integration variable. The integration of $\dot{F}$ and $\dot{S}$ are analogous and produce the external work and the cohesive work, respectively:

$$F = \int_0^T \dot{F} \mathrm{d}t \tag{4}$$

$$S = \int_0^T \dot{S} \mathrm{d}t \tag{5}$$

A classical switch of the derivatives from time t to area s of the active part of Γ_c, Γ_{c_a}, results in the following identity:

$$\frac{\mathrm{d}S}{\mathrm{d}s} = \frac{\mathrm{d}W}{\mathrm{d}s} - \frac{\mathrm{d}F}{\mathrm{d}s} \tag{6}$$

Standard arguments result in the following definition for the strain energy release, J:

$$J = -\frac{\mathrm{d}S}{\mathrm{d}s} = \frac{\mathrm{d}\left(F - W\right)}{\mathrm{d}s} \tag{7}$$

For elasto-plastic materials, we must acknowledge that part of the energy released from the crack advance was already dissipated by the plastic deformation process and therefore must be subtracted from the fracture energy:

$$J = J_R - W_p \Rightarrow \text{crack growth} \tag{8}$$

where J_R is the LEFM fracture energy (or critical energy release rate) for the considered material and geometry. In (8), W_p is the plastic deformation work, given as:

$$W_p = \int_0^T \boldsymbol{\sigma} : \dot{\boldsymbol{\varepsilon}}_p \mathrm{d}t \tag{9}$$

where $\dot{\boldsymbol{\varepsilon}}_p$ is the plastic strain rate. Finite element technology makes use of standard constant-strain triangles and isoparametric quadrilaterals, as well as our shell elements (cf. [13, 11]). A further note is required: traditionally, we use the MINI element (cf. [17]), see also [16], for near-incompressible problems. However, for plane-stress problems we do not require a specialized formulation, so that displacement-based elements are used.

3 Specific techniques for modeling crack growth

3.1 Virtual crack closure

The determination of stress intensity factors can be performed by a variety of well-known methods (cf. [19]). All of these methods calculate the same configurational derivative (cf. [26]). The most established method is the contour $J-$integral. We have recently used contour integrals with success (see [62]) in the context of configurational forces. However, there are some shortcomings of $J-$integrals for multiple cracks and the support function requires a user-defined radius. An alternative is the virtual crack closure technique by Ribicki [57] and further developed by Krueger [40]. Furthermore, since it is based on the crack tip opening displacement (CTOD) and it is known to have high predictive capabilities for large strain plasticity [43, 60]. A short summary of the application by Krueger is provided here. Using a local frame corresponding to the classical fracture mode decomposition (the mode frame), we can determine the transformation matrix whose rows are three orthogonal directions corresponding to each mode relative displacement:

$$\boldsymbol{T}_{\text{mode}} = \begin{bmatrix} \hat{\boldsymbol{e}}_I^T \\ \hat{\boldsymbol{e}}_{II}^T \\ \hat{\boldsymbol{e}}_{III}^T \end{bmatrix} \tag{10}$$

where

$$\hat{\boldsymbol{e}}_{III} = \boldsymbol{n} \tag{11}$$

$$\boldsymbol{e}_{II}^{\star} = \left[\boldsymbol{x}_0 - \left(\frac{\boldsymbol{x}_1 + \boldsymbol{x}_2}{2}\right)\right] \tag{12}$$

$$\boldsymbol{e}_{II} = \left(\boldsymbol{I} - \boldsymbol{n} \otimes \boldsymbol{n}\right) \boldsymbol{e}_{II}^{\star} \tag{13}$$

and

$$\hat{\boldsymbol{e}}_I = \hat{\boldsymbol{e}}_{III} \times \hat{\boldsymbol{e}}_{II} \tag{14}$$

The classical notation for unit vectors obtained by the Euclidian norm is adopted:

$$\hat{\bullet} = \frac{\bullet}{\| \bullet \|_2} \tag{15}$$

The relative displacement for the mode frame is given by:

$$[[\boldsymbol{u}]] = \left\{ \begin{array}{c} u_I \\ u_{II} \\ u_{III} \end{array} \right\} = \boldsymbol{T}_{\text{mode}} \left(\boldsymbol{u}_2 - \boldsymbol{u}_1 \right) \tag{16}$$

and the internal forces at the tip are obtained by assembling elements above the predicted crack segment:

$$\left\{ \begin{array}{c} f_I^+ \\ f_{II}^+ \\ f_{III}^+ \end{array} \right\} = \boldsymbol{T}_{\text{mode}} \boldsymbol{f}_{0i}^+ \tag{17}$$

where $\boldsymbol{f}_{0i}^+$ are the internal forces assembled from elements identified as + in Figure 1 at the tip node (node 0). Note that a partition of the regions ahead of the crack tip is necessary to obtain the correct values for the internal forces.

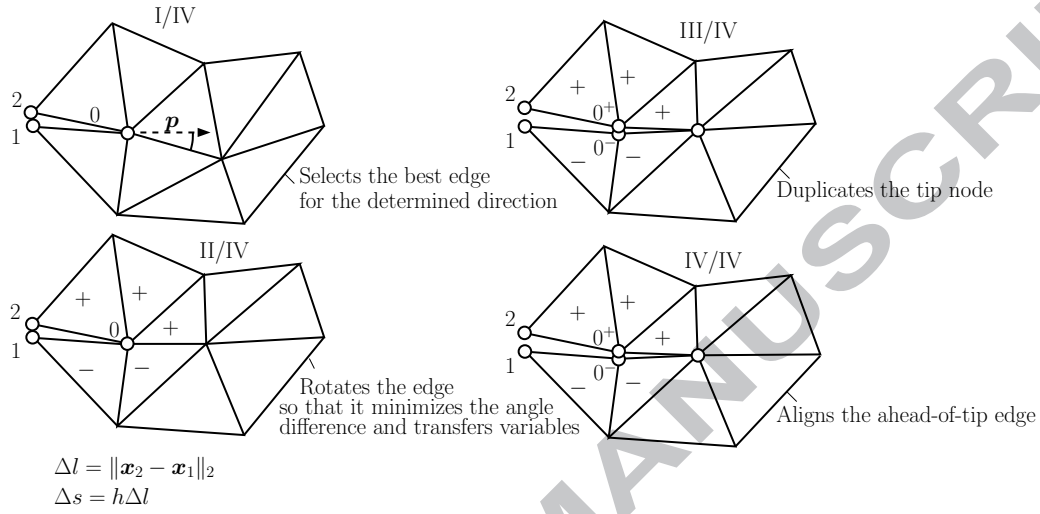

Figure 1: Edge-based crack propagation algorithm for shells.

Predicted fracture energies follow the classical derivation by Krueger (s identified in Figure 1):

$$J_I = \frac{1}{2\Delta s} f_I^+ u_I \tag{18}$$

$$J_{II} = \frac{1}{2\Delta s} f_{II}^+ u_{II} \tag{19}$$

$$J_{III} = \frac{1}{2\Delta s} f_{III}^+ u_{III} \tag{20}$$

The condition for crack advance in brittle cases results from the energy sum corresponding to (8):

$$J_I + J_{II} + J_{III} = J_R \tag{21}$$

The crack path orientation follows our previous approach ([9]). For plane problems and for shells, the crack path has only components along $\hat{\boldsymbol{e}}_I$ and $\hat{\boldsymbol{e}}_{II}$ and the Ma-Sutton criterion [43, 60] is adopted to predict it:

$$\boldsymbol{p} = \hat{\boldsymbol{e}}_1 \sin(\theta_c) + \hat{\boldsymbol{e}}_2 \cos(\theta_c) \tag{22}$$

where the angle θ_c is obtained as:

$$\theta_c = \begin{cases} \frac{-36.5\pi}{180} \arctan(2.2\alpha), & |\alpha| < \alpha_c \\ \frac{57.3\pi}{180} \cos(\alpha) \frac{\alpha}{|\alpha|} & |\alpha| \geq \alpha_c \end{cases} \tag{23}$$

$\alpha = \arctan\left(\frac{u_{II}}{u_I}\right)$. For the cohesive fracture modeling, it is important to note that crack path is still determined by this analysis *prior to the cohesive stage*. Determination of crack paths for problems with cohesive forces present difficulties (see [50]) circumvented by this technique. Figure 2 succinctly represents the proposed algorithm in flowchart form.

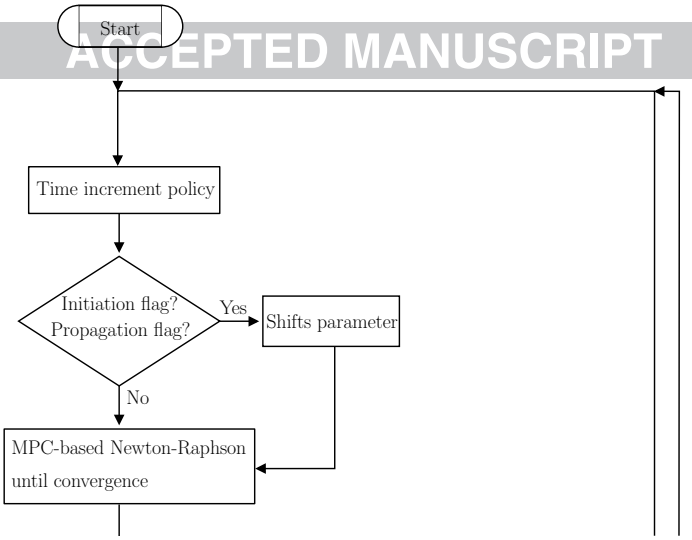

Figure 2: Initiation and propagation flowchart.

3.2 Cohesive discretization

The representation of the finite-displacement cohesive element makes use of a simple node/node arrangement as depicted in Figure 3. This approach is simpler than the node/edge method and it is sufficient for our purposes where only moderate displacements are present. In addition, the surface Patch test is satisfied. We consider all external edges (i.e. with only one underlying solid element) as candidates.

3.3 Consistent mixed-mode traction separation law

To introduce the decohesion process, an elastic damage traction-separation law is adopted. It depends on four constitutive properties: f_t, J_R, β and *tol* which are the tensile strength, the fracture energy, modes II and III parameter and the kinematical tolerance, respectively. It is a variation of the law proposed by Alfaiate *et al.* [1], able to deal with unloadings/reloadings with negative u_I. It is characterized by the closure effect, mixed mode damaging effect and purely elastic unloading. For the interested reader, a thorough discussion of cohesive representations is provided in the paper by Elices *et al.* [33]. The damage variable is denoted as d; normal stresses and tangential stresses are denoted as σ, τ_{II} and τ_{III}, respectively, and are grouped in the following traction vector $\boldsymbol{t}$:

$$\boldsymbol{t} = \left\{ \begin{array}{c} \sigma \\ \tau_{II} \\ \tau_{III} \end{array} \right\} = (1-d)\exp(1)\frac{f_t}{\kappa_0} \left\{ \begin{array}{c} a u_I + \kappa_0 \\ \beta u_{II} \\ \beta u_{III} \end{array} \right\} \tag{24}$$

where u_I, u_{II} and u_{III} are now extended to the discontinuity region and a is the crack closure parameter. The damage parameter depends on a kinematical variable, κ, according to the following law:

$$d = 1 - R^{-1}\left(1 + \alpha R - \alpha\right) e^{\alpha(1-R)-1} \tag{25}$$

with

$$R = \frac{\kappa + \kappa_0}{\kappa_0} \tag{26}$$

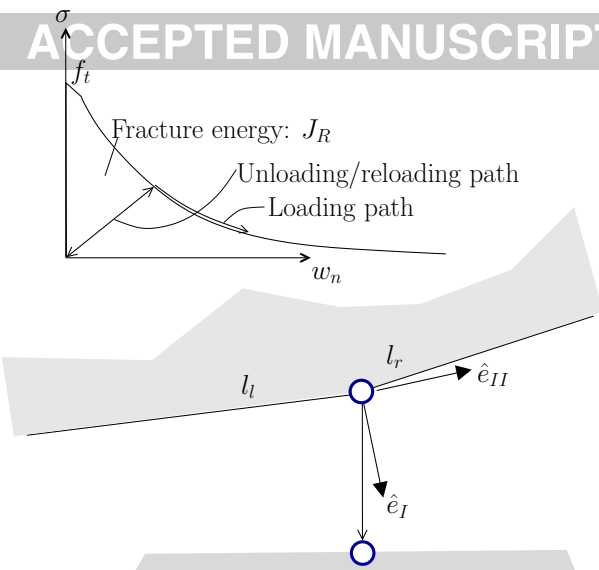

Figure 3: Node/node cohesive element for finite displacements.

and

$$\alpha = \frac{2 f_t \kappa_0}{J_R} \tag{27}$$

where κ_0, the kinematical shift, is introduced to avoid the initial infinite slope. The kinematical variable κ can be viewed as the "equivalent opening," a quantity to be defined by *complementarity* conditions. We use a non-dimensional kinematic tolerance, tol, to define κ_0:

$$\kappa_0 = 2\text{tol}\frac{J_R}{f_t} \tag{28}$$

The crack closure parameter is a function of the opening sign:

$$a = \begin{cases} 1, & u_I \geq 0 \\ \frac{1}{1-d}, & u_I < 0 \end{cases} \tag{29}$$

this allows a fixed slope for contact and keeps the tangential stress unaltered when penetration occurs. The evolution of κ is *implicitly* defined by the following complementarity conditions:

$$\begin{aligned} \dot{d} &\geq 0 \\ \dot{d}\phi &= 0 \\ \phi &\leq 0 \end{aligned} \tag{30}$$

with the fracture surface being given as the following difference:

$$\phi = < u_I > + \beta u_t - \kappa \tag{31}$$

with $u_t = \sqrt{u_{II}^2 + u_{III}^2}$. This simple mixed-mode law and the related kinematical shift were found to be appropriate for the examples under study, although complete solutions to this class of problems resort to the concept of set-valued forces [36, 12]. A representation of this law is given for several values of u_I and u_{II} in Figure 4. In all examples we use $tol = 1 \times 10^{-3}$.

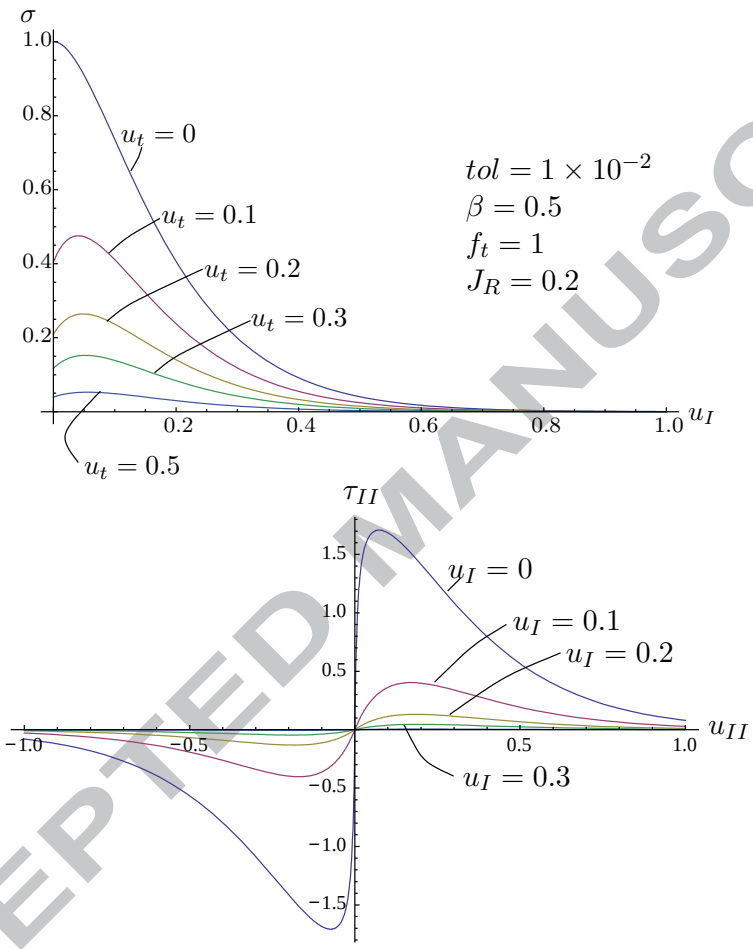

Figure 4: Mixed-mode cohesive law in loading. Unloading occurs to the origin.

3.4 Constraint-based solution control

The determination of the load (or displacement) factor Q either the energy release rate or the stress is constrained. A complete discussion of the solution constraint is given in Moës and Belytschko [45] and an extended procedure was introduced by Areias *et al.* [9]. If a load factor Q is included as an unknown, the system must be enlarged by appending the control constraint $s_c(\boldsymbol{u}) = 0$:

$$\begin{aligned} \boldsymbol{r}(Q,\boldsymbol{u}) &= \boldsymbol{0} && (32)\\ s_c(\boldsymbol{u}) &= 0 && (33) \end{aligned}$$

where $\boldsymbol{r}(Q,\boldsymbol{u})$ is the discrete equilibrium residual and $s_c(\boldsymbol{u})$ is the crack constraint. For proportional loading and we can write $\boldsymbol{r}(Q,\boldsymbol{u})$ as:

$$\boldsymbol{r}(\boldsymbol{Q},\boldsymbol{u}) = Q\boldsymbol{e} - \boldsymbol{i}(\boldsymbol{u}) \tag{34}$$

with, following classical notation, $\boldsymbol{e}$ is the total load vector and $\boldsymbol{i}$ is the internal force vector. Generalizations of (34) are straightforward but for the present applications appear unnecessary. The solution by Newton-Raphson iteration results in:

$$\begin{bmatrix} \boldsymbol{K}(Q,\boldsymbol{u}) & -\boldsymbol{e}(Q,\boldsymbol{u}) \\ \boldsymbol{l}(\boldsymbol{u}) & 0 \end{bmatrix} \begin{Bmatrix} \boldsymbol{u}_v \\ Q \end{Bmatrix} = - \begin{Bmatrix} \boldsymbol{i}(\boldsymbol{u}) \\ s_c(\boldsymbol{u}) \end{Bmatrix} \tag{35}$$

where $\boldsymbol{u}_v$ is the iterative correction to the displacement $\boldsymbol{u}$ and the load factor. In (35), the quantities $\boldsymbol{l}$ and $\boldsymbol{K}$ are the following derivatives:

$$\begin{aligned} \boldsymbol{l}(\boldsymbol{u}) &= \frac{\mathrm{d}s_c}{\mathrm{d}\boldsymbol{u}} && (36)\\ \boldsymbol{K}(Q,\boldsymbol{u}) &= \frac{\partial \boldsymbol{i}(Q,\boldsymbol{u})}{\partial \boldsymbol{u}} && (37) \end{aligned}$$

Defining $\boldsymbol{u}_i = \boldsymbol{K}^{-1}\boldsymbol{i}$ and $\boldsymbol{u}_e = \boldsymbol{K}^{-1}\boldsymbol{e}$, and subsequently $s_i = \boldsymbol{l}\cdot\boldsymbol{u}_i$, $s_e = \boldsymbol{l}\cdot\boldsymbol{u}_e$ we finally obtain:

$$\begin{aligned} Q &= \frac{s_i - s_c}{s_e} && (38)\\ \boldsymbol{u}_v &= Q\boldsymbol{u}_e - \boldsymbol{u}_i && (39) \end{aligned}$$

which provides the overall solution process for the constrained equilibrium. Of course, this procedure corresponds to an exact linearization if $\boldsymbol{l}$ is calculated in closed-form.

4 Computational fracture examples

Five classical quasi-brittle problems are tested. Assessment makes use of comparisons with experiments found in the literature and with alternative formulations. Specifically, the phase field approach to brittle fracture is also used for comparison in one of the examples (cf. Van Goethem and co-workers [3]). In addition, the XFEM implementation by Dias-da-Costa *et al.* [31] is used as a comparison.

4.1 Brittle fracture of a thin aluminum plate

With the purpose of inspecting the mesh size effect on both crack path and load/deflection results, we contemplate an Aluminum plate with a pre-existing crack (created with a metal saw and with its tip sharpened by a razor blade). Relevant data for this problem is shown in Figure 5. The experimental setup and final result are also shown in the same Figure. The experiment shows considerable plastification at the resistant region of the plate. However, for this example we do include this ingredient and it was found to be of little effect in the crack trajectory for the planified plate. Crack paths for three meshes of triangular shell elements are presented in Figure 6 along with the planified experimental crack path. It can be observed that there is a reasonable agreement with the experimentally verified path. A comparison of required forces for three meshes

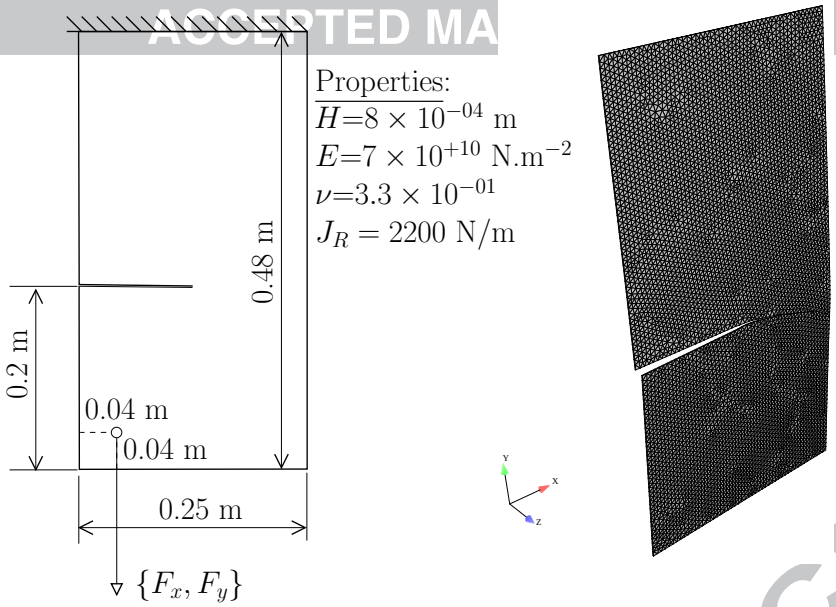

(a) Geometry, properties and crack path representation on the plate.

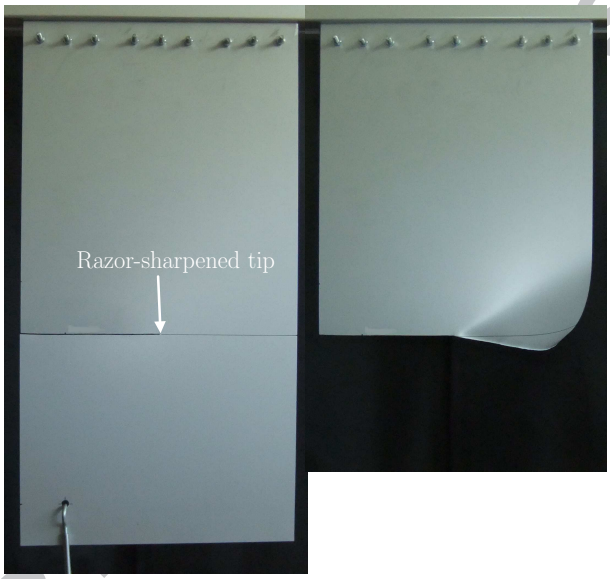

(b) Experimental setup and final result.

Figure 5: Thin aluminum plate: geometry, dimensions and relevant material properties. The experimental figures are also shown.

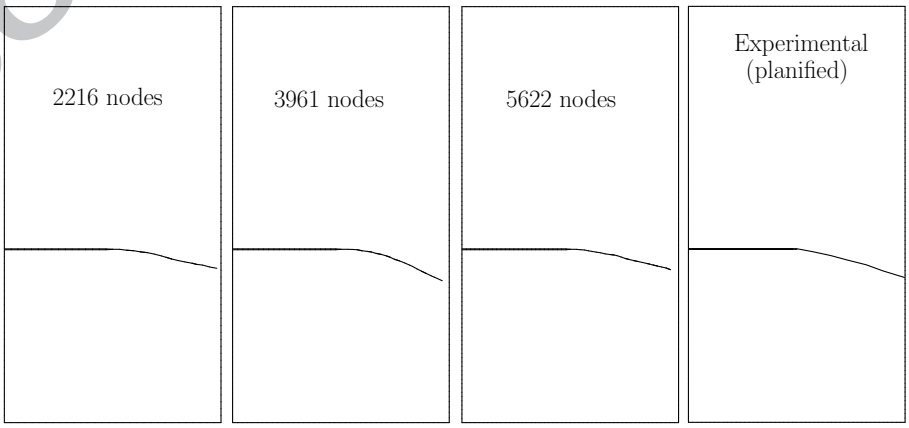

Figure 6: Thin aluminum plate: numerical crack paths for three triangular meshes and the experimental result.

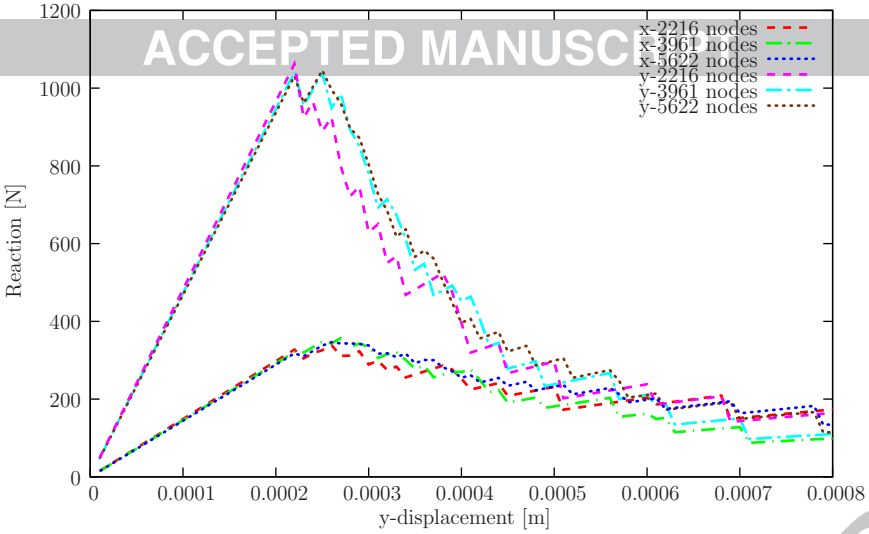

Figure 7: Thin aluminum plate: reactions vs. imposed displacement components for the three triangular meshes.

with triangular shell elements is shown in Figure 7. Irregularities in the force/displacement results appear due to the effect of brittle decohesion and are attenuated with mesh refinement.

For comparison, crack paths using the phase-field technique (which is an interesting competing method for brittle fracture) are shown in Figure 8. The fundamental reference for this method is provided by Allaire, Jouve and Van Goethem [3]. Two worth noting points must be stated:

- Finer meshes are required for a reasonable resolution when the phase-field model is used.
- There is a tendency for phase-field models to follow the mesh orientation.

Another aspect deserving inspection is the suitability of the present approach for the use with quadrilateral elements. Recent finite strain elements show improved performance for distorted quadrilateral elements and it is interesting to inspect the differences between triangles and quadrilaterals with non-structured meshes. Figure 9 shows this comparison (both the crack paths and the load/deflection results). Two conclusions worth mentioning are:

- Quadrilateral meshes show stronger mesh distortion at strained regions near the crack tip. Frequently three nodes become collinear.
- Quadrilateral meshes produce slightly less stiff results.

Note that, in contrast with triangular meshes, severely distorted quadrilateral meshes often fail to comply with the predicted crack path.

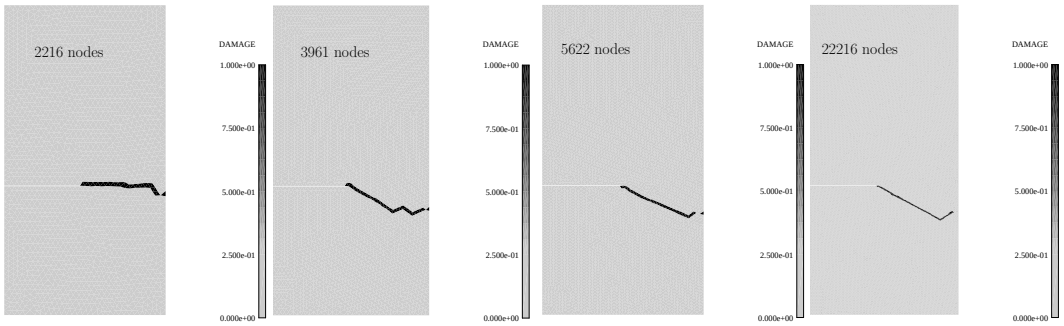

Figure 8: Thin aluminum plate: crack paths resulting from an alternative technique: the *phase-field* approach (see the implementation by Allaire, Jouve and Van Goethem [3]).

4.2 Bittencourt's drilled plate

We use the example by Bittencourt *et al.* [21] who performed experimental and numerical studies of curvilinear crack propagation. Specimens are built of Polymethylmethacrylate (PMMA) and use of finite strains are

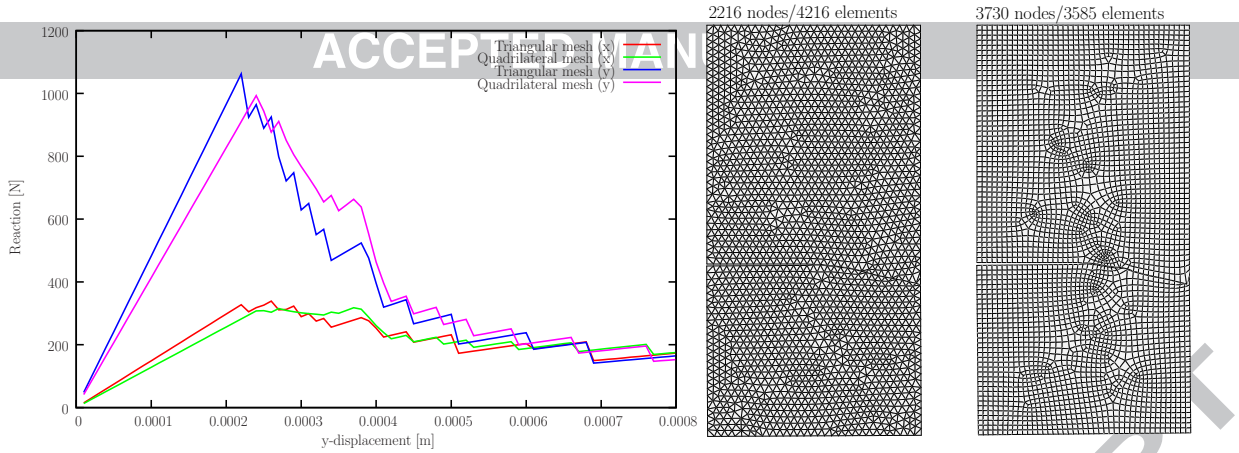

Figure 9: Thin aluminum plate: comparison between triangular and quadrilateral elements.

required (cf. [9]). Geometry, relevant material properties and boundary conditions are shown in Figure 10 for two specimens differing in the linear dimensions a and b. Figure 11 shows the results for Specimen 1 and a comparison with experimental crack paths. In the paper by Bittencourt [21], the Erdogan-Sih [34] fracture criterion was used, with stress intensity factors calculated with the domain-integral (see also [45] for a detailed discussion of this approach) and quarter-point elements. In that paper, the recursive spatial decomposition method was introduced to perform the mesh subdivision. We here avoid subdivision and test regular meshes of both triangles and quadrilaterals. Only specimen #1 required smaller elements in the turning region (for the coarser mesh, which was also a conclusion of Bittencourt *et al.*) in the crack turning region near the second hole. The presence of the three holes perturbs the stress fields making the crack trajectory very sensitive to the position and size of the existent notch. Despite previous well known accuracy difficulties (documented in [21] and observed in [44]), good agreement was observed between predicted and experimental crack paths (see Figure 11). The crack mouth opening displacement (CMOD) is used to control the solution and capture the snap-backs. Note that snap-backs are *common for low values of* J_R, as shown by Carpinteri [28] and further discussed by Moës and Belytschko [45]. Load-CMOD results are shown in Figure 13 for both specimens and load-deflection results are shown in Figure 14, showing the well-known snap-backs. Very smooth results are obtained and we reach small fracture energies without convergence problems. For two values of the fracture energy, $J_R = 1$ N/mm and $J_R = 10$ N/mm, the cohesive stresses are shown in Figure 15. These are perfectly smooth and hence, contrary to the purely brittle analyses, result in smooth behavior. A comparison between triangles and quadrilaterals is presented in Figure 12. If the quadrilateral mesh is sufficiently regular, results are similar to those with the triangular mesh.

A note is required concerning the mesh with 101541 elements: it is only used for comparison and its crack path is not more precise than the ones produced by coarser meshes.

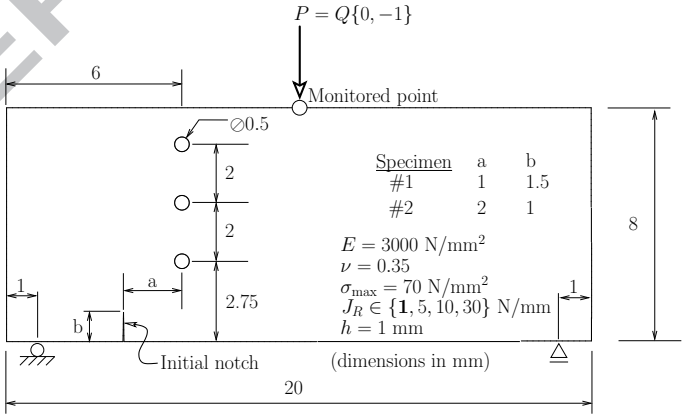

Figure 10: Relevant data for Bittencourt's drilled plate. geometry, boundary conditions and material properties. Geometry parameters a and b vary according to the specimen.

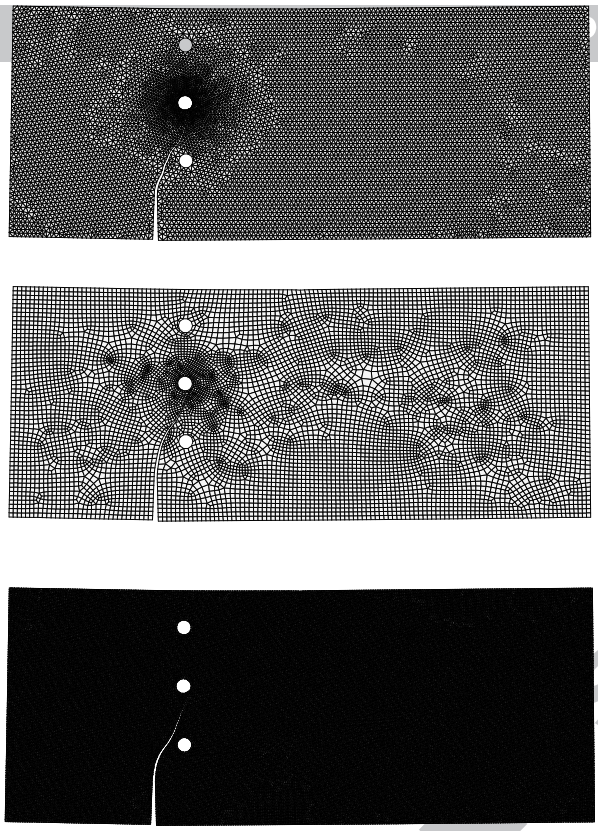

(a) Specimen #1 deformed mesh (triangles and quadrilaterals) with local refinement. Coarse triangular mesh contains 9126 nodes and 17812 elements and the coarse quadrilateral mesh contains 9062 nodes and 8841 elements. The uniform triangular mesh is also shown (51299 nodes and 101541 elements).

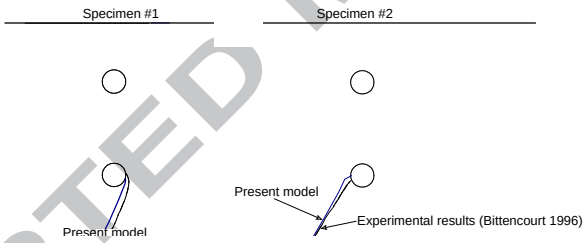

(b) Crack path comparisons with experimental results (cf. [21]).

Figure 11: Bittencourt's drilled plate: Results shown for specimen #1.

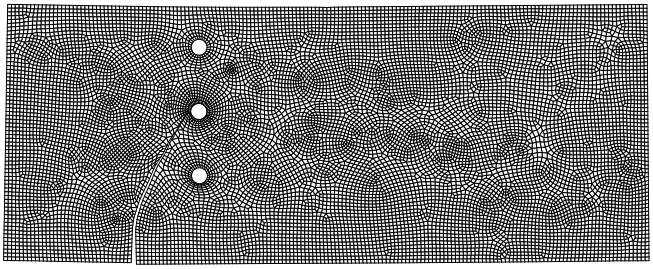

Figure 12: Bittencourt's drilled plate. Results shown for specimen #2 with a quadrilateral mesh containing 12565 elements and 12850 nodes.

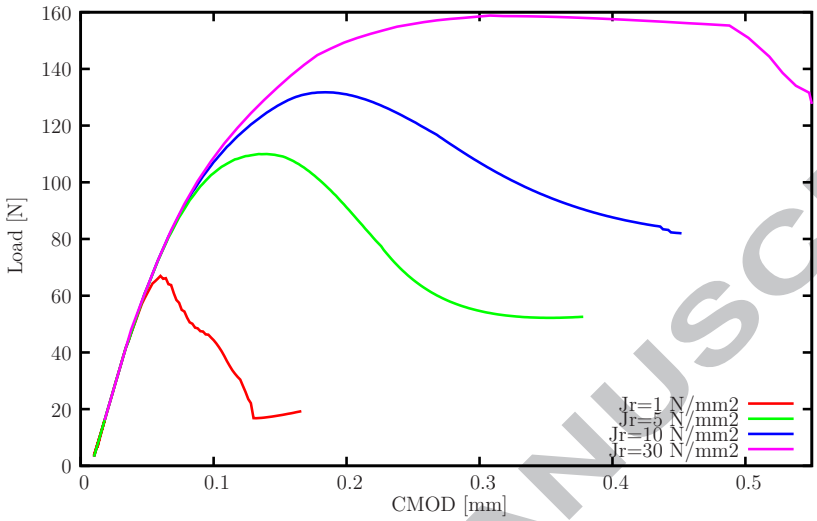

(a) Specimen #1

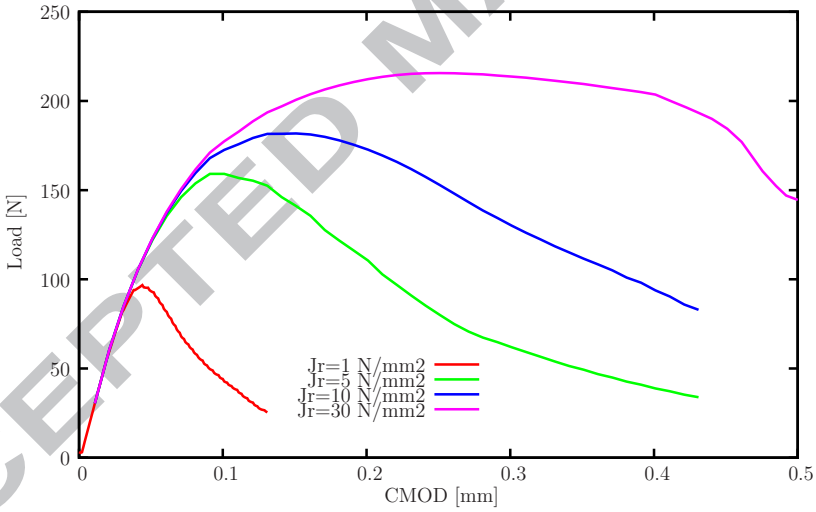

(b) Specimen #2

Figure 13: CMOD/Load results for the two specimens.

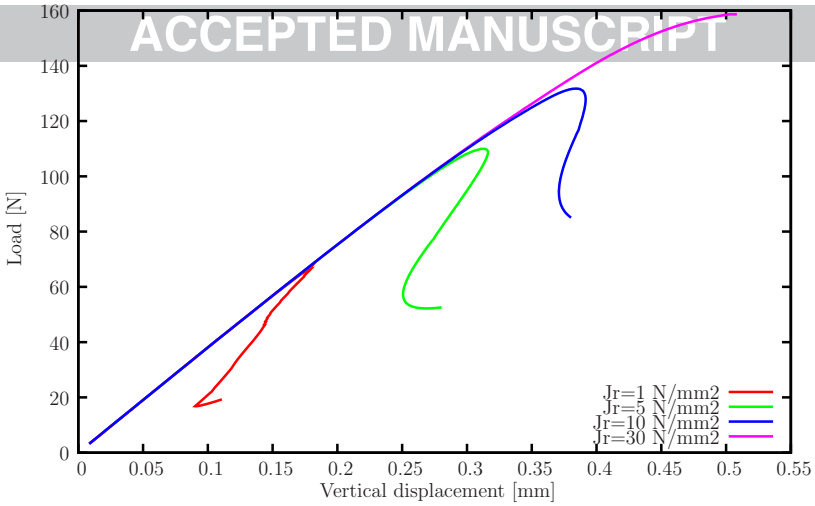

(a) Specimen #1

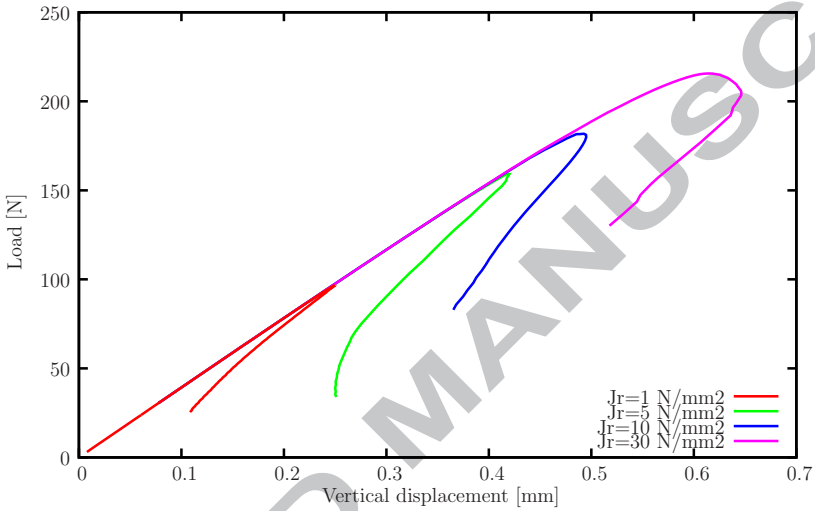

(b) Specimen #2

Figure 14: Displacement under the point Load/Load results for the two specimens.

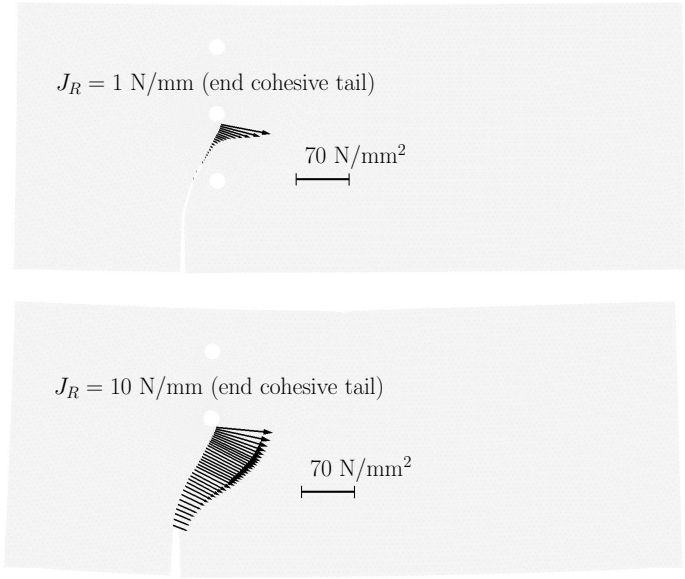

Figure 15: Specimen #1: cohesive tails for $J_R = 1$ N/mm and $J_R = 10$ N/mm. Similar tails are obtained for specimen #2.

4.3 Single edge notched beam

The single edge notched (SEN) beam introduced by Schlangen (cf. [58]) is now explored. A description of this problem, with material properties and boundary conditions is presented in Figure 16. Three uniform triangular meshes with different number of nodes are tested, containing 2939, 5185 and 11514 nodes. The arc-length method (see subsection 3.4) is used, with monotonically increasing CMSD (crack mouth sliding displacement). The crack path reproduces closely the experimental envelope, as can be observed in Figure 17; even near the support the experimental observations are accurately reproduced. A comparison with the experimental results and the DSDA method [1, 8], along with a study of mesh and step size influence is effected. As can be observed in Figure 18, after the peak load is reached, the numerical results are more brittle than the experimental results. According to [2], this is due to the fact that an isotropic mode-I traction-jump law is used. The results are immune to the step-size up to very large CMSD increments.

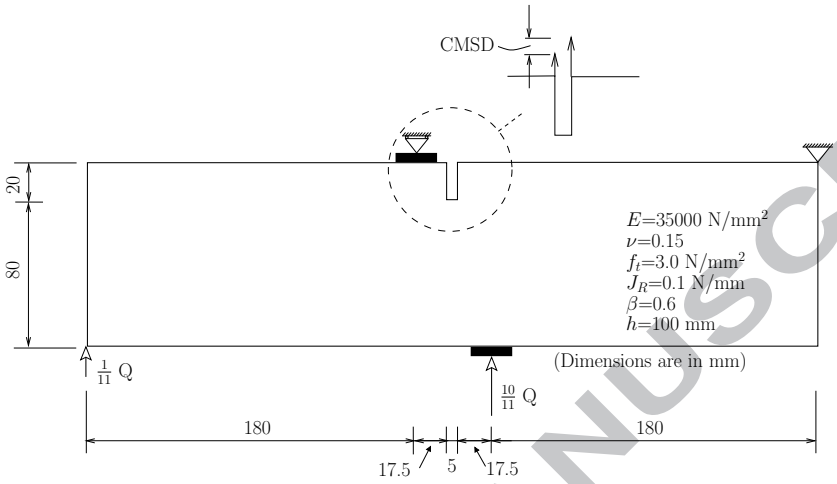

Figure 16: Schlangen's SEN test: geometry, boundary conditions and material properties.

4.4 Gravity dam scale model

This problem is one of the scale model dam problems solved (and tested) by Barpi and Valente (cf. [18]). We use a 150 mm pre-crack in a model dam with the scale 1 : 40 as described in that reference (note that there is also a specimen with a 300 mm pre-crack). A hydrostatic load is applied to the left face of the dam and self-weight is considered (this is replaced by a set of forces in the original work). Figure 19 presents the geometry, dimensions, loading and properties defining this problem. Also shown is a comparison with both experimental and numerical crack trajectories reported by Barpi and Valente. Two meshes are used (composed solely of triangles) containing 3904 nodes and 8707 nodes. The latter has a better agreement with the experimental crack path, as can be observed in Figure 19. We also show the CMOD/load results compared with the ones reported by Barpi and Valente and the GFEM results by Dias-da-Costa *et al.* [31] in Figure 20. Note that, in that work, the mesh is refined near the crack tip. Cohesive tails and principal normal stresses are shown for the two meshes in Figure 21.

4.5 Cohesive crack growth in a four-point bending concrete beam

The four-point bending concrete beam problem consists of a bi-notched concrete beam subjected to two point loads. It was initially presented by Bocca *et al.* [22] and numerically tested by a multitude of authors. The effect of size is apparent since two specimens with different dimensions are tested. In the original work [22], an experimental setting is described in detail. From the set of specimens studied by Bocca *et al.* we only retain the specimens with $c/b = 0.8$, $b = 50$ and $b = 200$ mm, since only these have useful experimental data. In addition to these results, we are also concerned with the crack paths that were reported in [22]. Using the well-known cracking particle method, Rabczuk and Belytschko [54] obtained excellent results for the crack path prediction, although the load in the load-displacement diagram was higher than the experimental one. In addition, with the particle methods, there is the problem of selecting the support dimension in the crack region. We use a single *uniform* mesh, with 11599 nodes and 22656 triangular elements. All relevant data is shown in Figure 22. For anti-symmetry reasons, we force the same mouth horizontal displacement at the edge of notches A and B: $\Delta u_B = \Delta u_A$. It has been debated if quasi-static simulations allow propagation of more than one crack (see the excellent thesis by Chaves e.g. [29]) . We obtain an excellent agreement with the experimental crack paths,

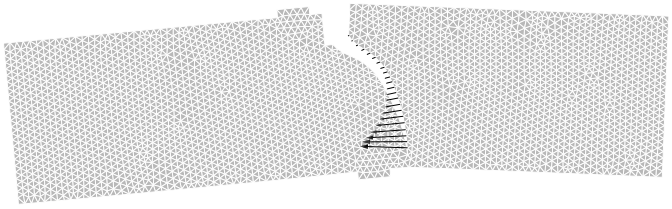

(a) 2939 nodes and 5616 elements (100× magnified). Normal cohesive stress is represented.

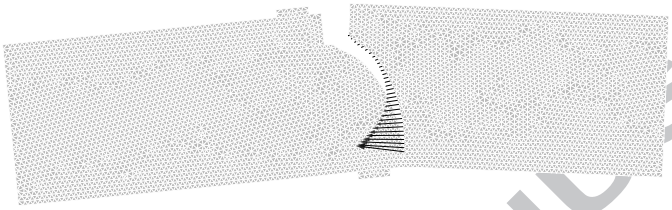

(b) 5185 nodes and 10014 elements (100× magnified). Normal cohesive stress is represented.

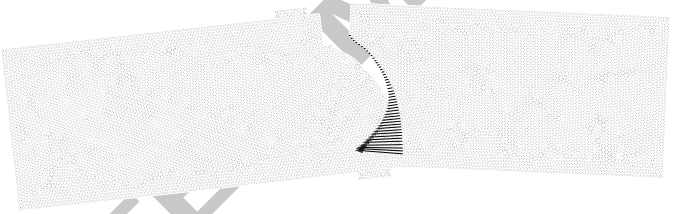

(c) 11514 nodes and 22498 elements (100× magnified). Normal cohesive stress is represented.

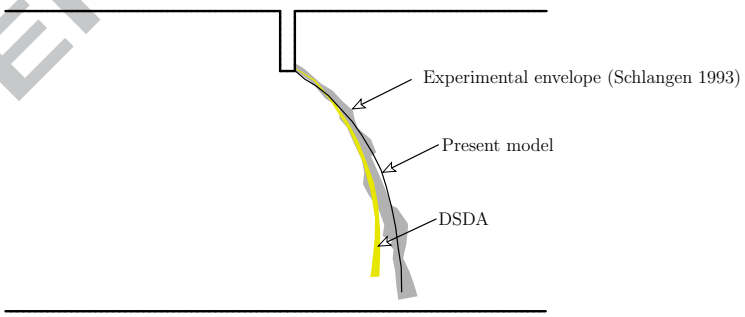

(d) Crack path comparison

Figure 17: Schlangen's SEN test: Deformed meshes for the 3 cases are shown, with 5616, 10014 and 22498 elements. Crack path (10014 elements) compared with DSDA [32] (yellow) and the experimental results by Schlangen [58].

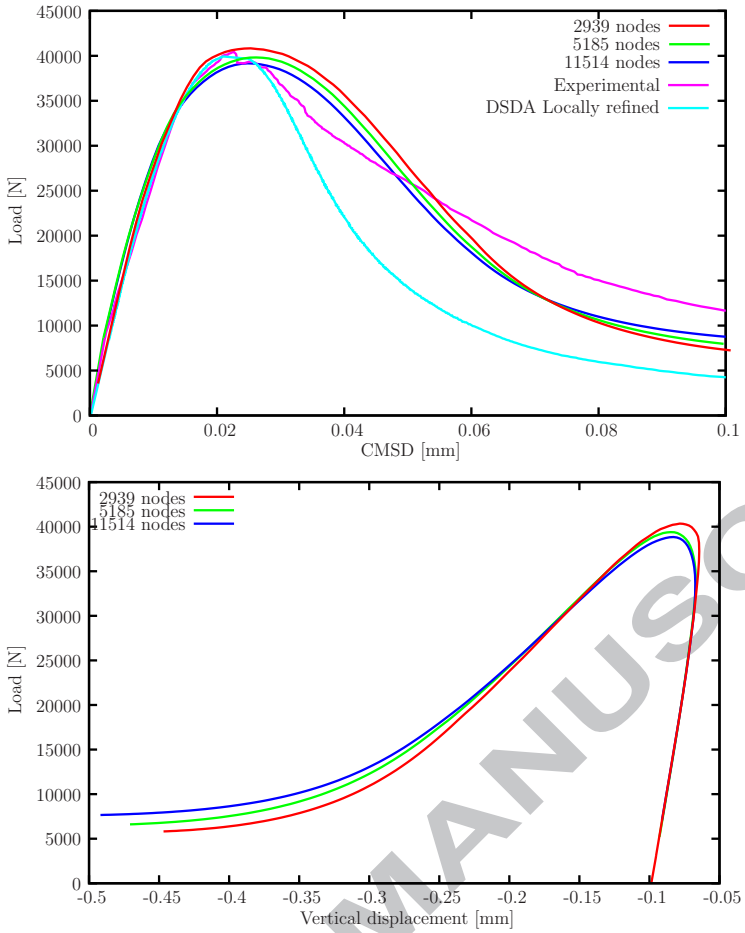

Figure 18: Schlangen's SEN test: load-CMSD results: comparison with the experimental results by Schlangen [58] and the DSDA technique [32].

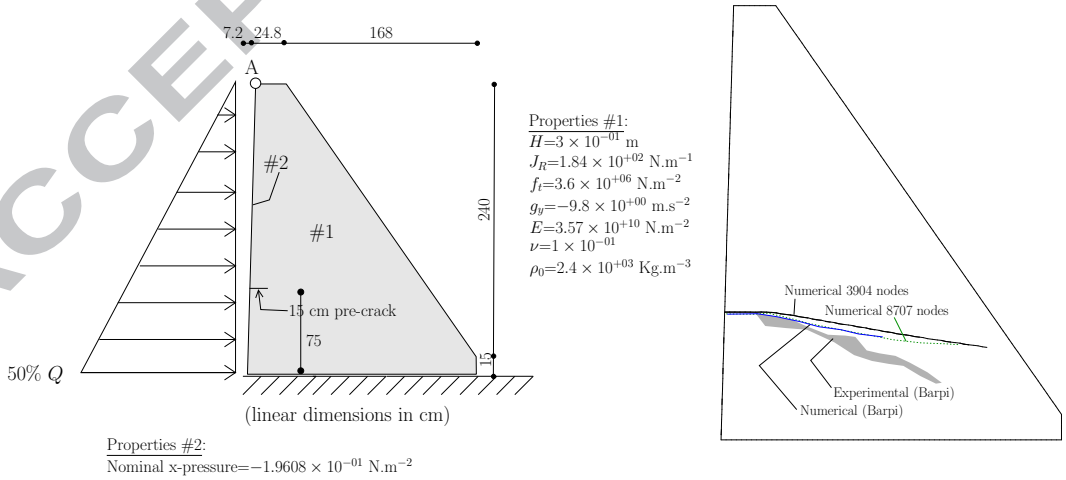

Figure 19: Gravity dam geometry and relevant data. Crack path comparison with the results from Barpi and Valente [18].

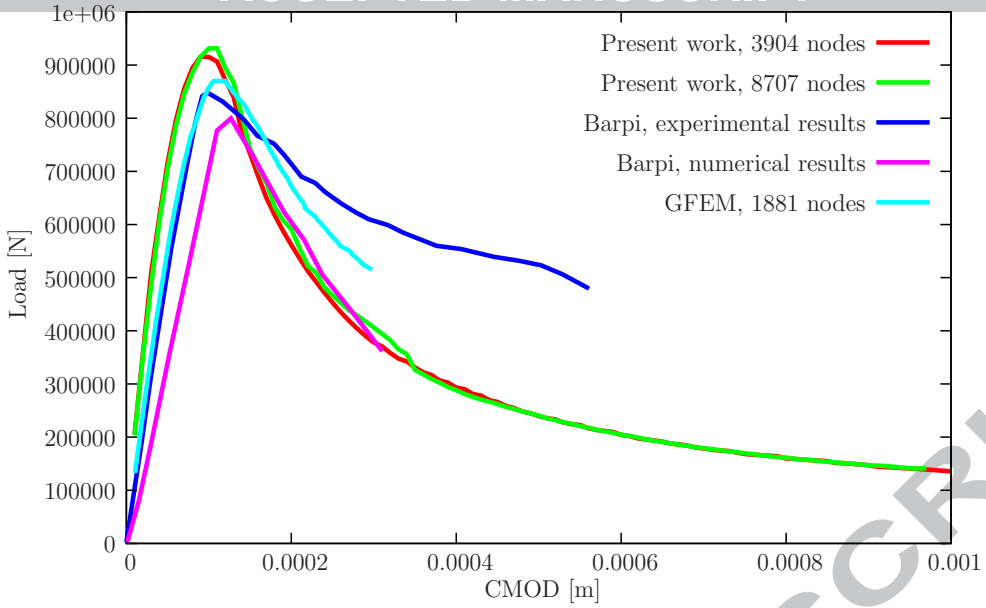

Figure 20: Gravity dam CMOD/load results. A comparison with the results reported by Barpi and Valente [18] and Dias-da-Costa *et al.* [31] is shown.

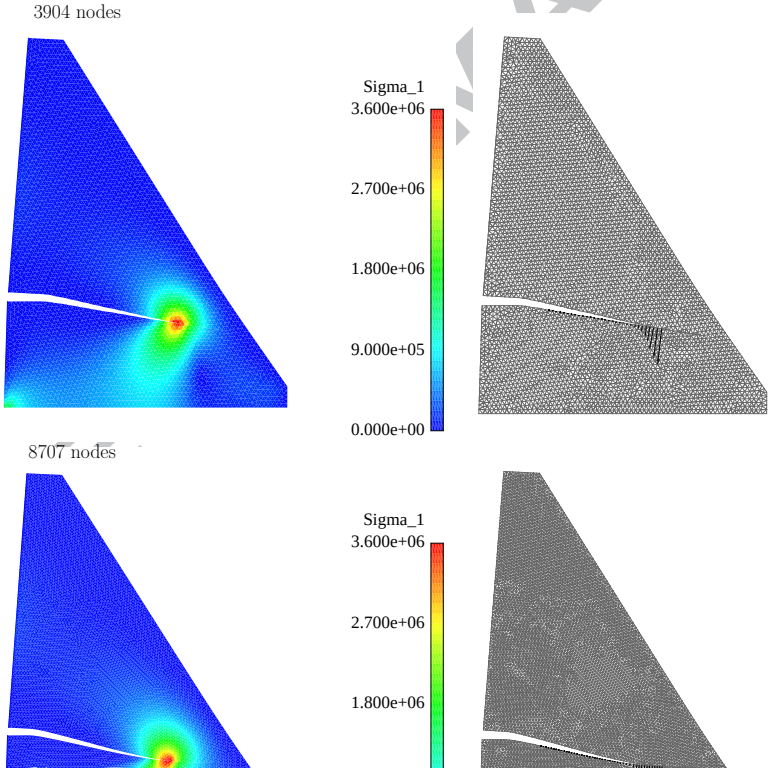

Figure 21: Gravity dam. Principal stress contour plots and cohesive tails (100× magnified).

as shown in Figure 23. The relatively wide spread of experimental crack paths is typical and results from the use of 6 specimens of reference [22]. Experimentally, some residual crack evolution in the opposite direction of the final path was observed and we also obtained that effect. Load-displacement results are shown in Figure 24 where a comparison with the measurements of Bocca *et al.* [22] and the cracking particle method of Rabczuk and Belytschko [54] is made. For the smaller specimen there is a somehow longer and lower curve than the observed one.

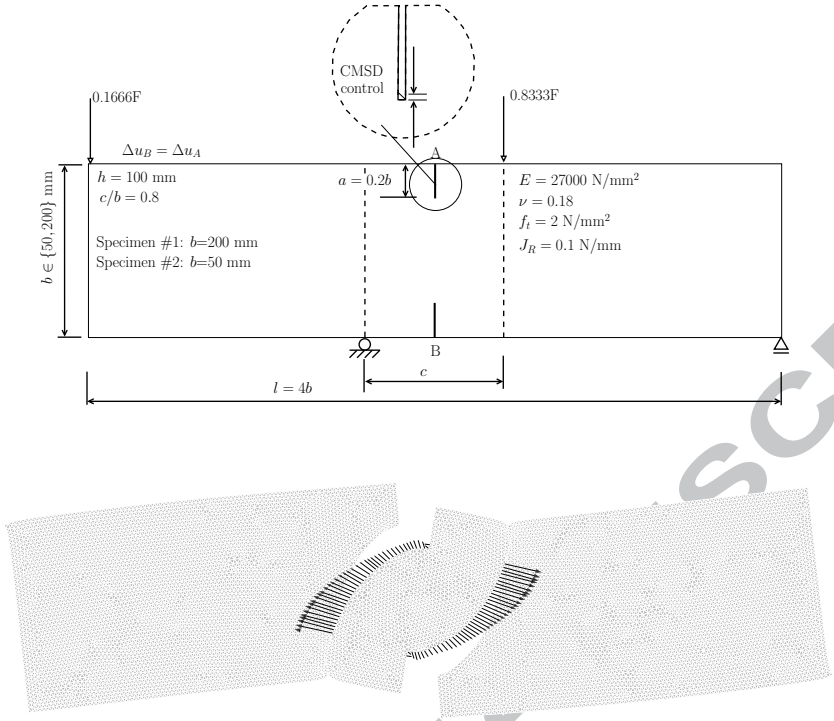

Figure 22: Four-point bending of a concrete beam: geometry, boundary conditions, multipoint constraints ($\Delta u_B = \Delta u_A$) and material properties. Also shown is the final deformed mesh 50× magnified with the attached cohesive stress vectors.

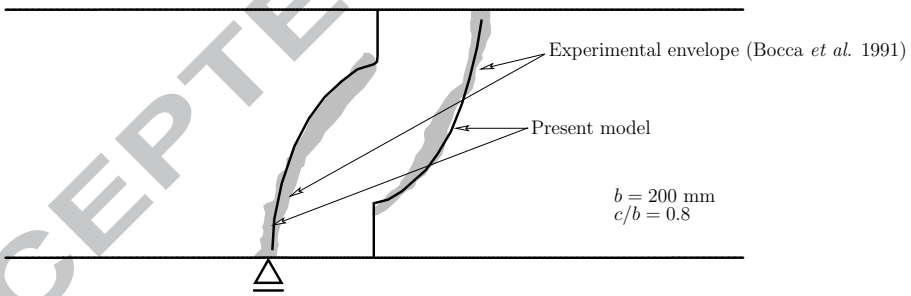

Figure 23: Four-point bending of a concrete beam: crack paths compared with the envelope of experimental results by Bocca, Carpintieri and Valente [22].

4.6 Mixed-mode ARCAN fixture

The ARCAN fixture was used by Sutton *et al.* [60] in a crucial work on mixed-mode nonlinear Fracture Mechanics. Specifically, the transition between mode I and II for Aluminum alloys and the corresponding crack kinking angle were determined. This test is applied here to assess the crack path accuracy. We use our recent algorithm for finite strain plasticity (cf. [10]) with a two yield surface criterion to include the progressive contraction of the tensile yield stress in ductile fracture. The finite strain elasto-plastic model is the two yield surface described in [10] and in [16], dependent on the void fraction f:

$$\sigma_{\text{eq}_1} = \frac{\sqrt{I_1^2 - 3I_2} - fc_1 I_1}{1 - f} \tag{40}$$

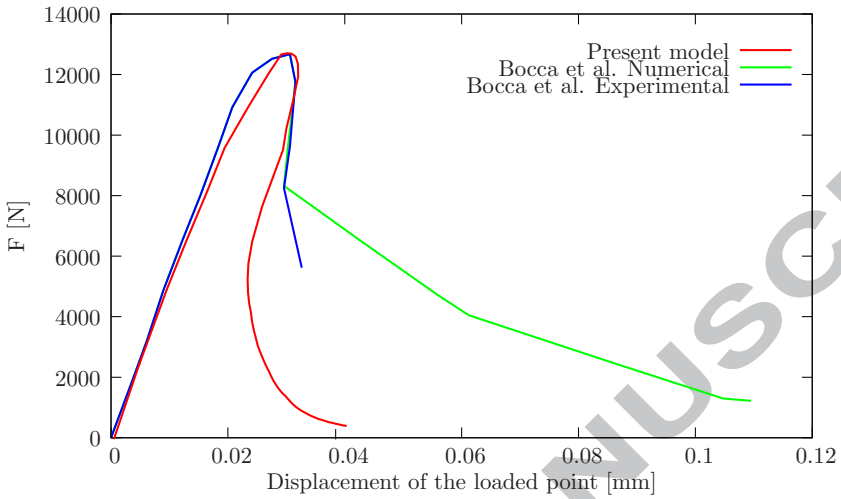

(a) $b = 50$ mm

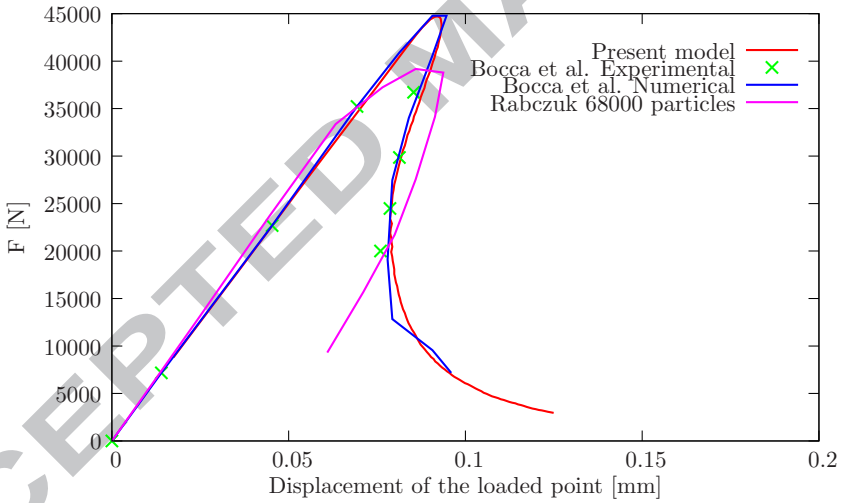

(b) $b = 200$ mm

Figure 24: Load-displacement results, compared with the results of Bocca *et al.* [22] and the cracking particle method of Rabczuk and Belytschko [54] (for the case $b = 200$ mm) with their 68000 particle analysis.

$$\sigma_{\text{eq}_2} = \frac{\sqrt{I_1^2 - 3I_2}}{1-f} \tag{41}$$

where the inequalities hold:

$$\phi_i \leq 0 \quad i = 1, 2 \tag{42}$$

with $\phi_i = \sigma_{\text{eq}_i} - \sigma_y$. σ_y is the yield stress, given by the hardening law. In (40) and (41) the following notation is used:

$$I_1 = \text{tr}\boldsymbol{\sigma} \tag{43}$$

$$I_2 = \frac{1}{2}\left[I_1^2 - \text{tr}\boldsymbol{\sigma}^2\right] \tag{44}$$

$$c_1 = 3\left(\frac{\sigma_{yc}}{\sigma_{yt}} - 1\right) \tag{45}$$

$$f = \max_{\text{history}} \left(\frac{\varepsilon_1}{\varepsilon_{\max}}\right)^2 \tag{46}$$

with σ_{yc} being the effective compressive Cauchy stress for $f = 1$, σ_{yt} is the tension Cauchy stress for $f = 1$ and ε_1 is the maximum principal Almansi strain with $\varepsilon_{\max}$ being a constitutive property. Further details are given in previous works [10] and [16].

Five values of the angle Φ are employed in the test: $\pi/12$, $\pi/6$, $\pi/4$, $\pi/3$ and $\pi/2$. Figure 26 shows a comparison with the experimental results of Sutton *et al* [60]. Reasonable agreement can be observed for all angles. In terms of reactions, Figure 27 shows the results for the studied angles. Higher values than those reported in [60] were obtained. However, further details on strain softening behavior were not given in that reference.

4.7 Pressure vessel fracture with slot

This problem was studied by R. Kitching and K. Zarrabi [39] with the main objective of evaluating the limit pressure of a cylindrical pressure vessel including the weakening effect of a thin rectangular slot at mid-height. The vessel is made of BS 1476 HT30WP Aluminum alloy. For this problem, both elasto-plastic and fracture properties are unambiguously defined in that reference. Specifically, in [39] the Authors assessed 12 specimens with distinct dimensions so that a systematic result could be obtained. We here concentrate on their specimen #12 for comparison purposes. Remaining relevant data is shown in Figure 28. Units correspond, in the original paper, to the British Imperial System but for uniformity we indicate them as "consistent". Our recent corotational shell element is adopted [11] with multiplicative plasticity (cf. [10]). In the lack of a better information, we use J_2 plasticity without damage. Initiation criterion is the critical effective plastic strain using a fitting of the results in the original reference ($\varepsilon_{\max} = 0.21$) and advance criterion is obtained from the subsequent J_R value and the VCCT. A mesh containing 2965 nodes and 5873 corotational elements (cf. [11]) is used (see the final configuration in Figure 29). A comparison with the experimental results by R. Kitching and K. Zarrabi is presented in Figure 30. Adequate correspondence can be observed, despite the complexity of the original problem. Examples such as the ones in the Areias and Belytschko work (cf. [6, 15, 7]) are now being successfully solved with this technique.

$E = 73.1$ GPa
$\nu = 0.33$
$\sigma_y = 344 + 769.44\overline{\varepsilon}_p$ Mpa for $\overline{\varepsilon}_p \leq 0.18$
$\sigma_y = 483 + 45.122(\overline{\varepsilon}_p - 0.18)$ Mpa for $\overline{\varepsilon}_p > 0.18$
$\varepsilon_{\max} = 0.18$
$h = 2.3$ mm
$m = 2$
$f_{\text{crit}} = 0.2$

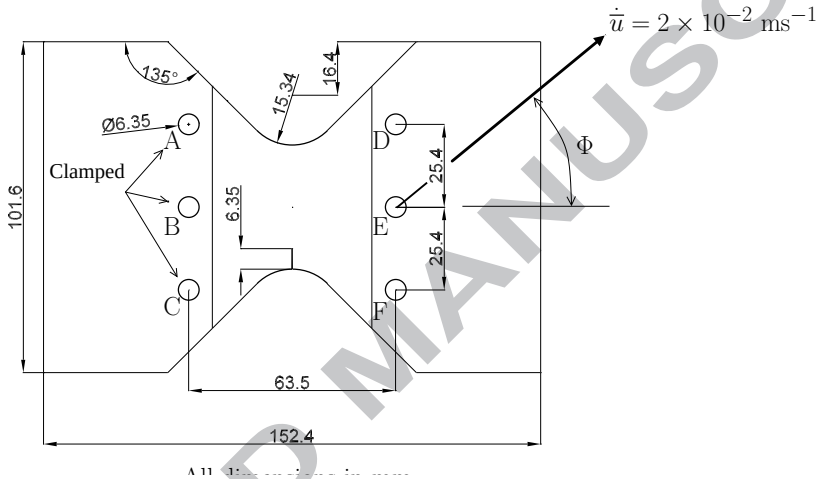

Figure 25: ARCAN test: relevant data. Further details are given in the original reference [60].

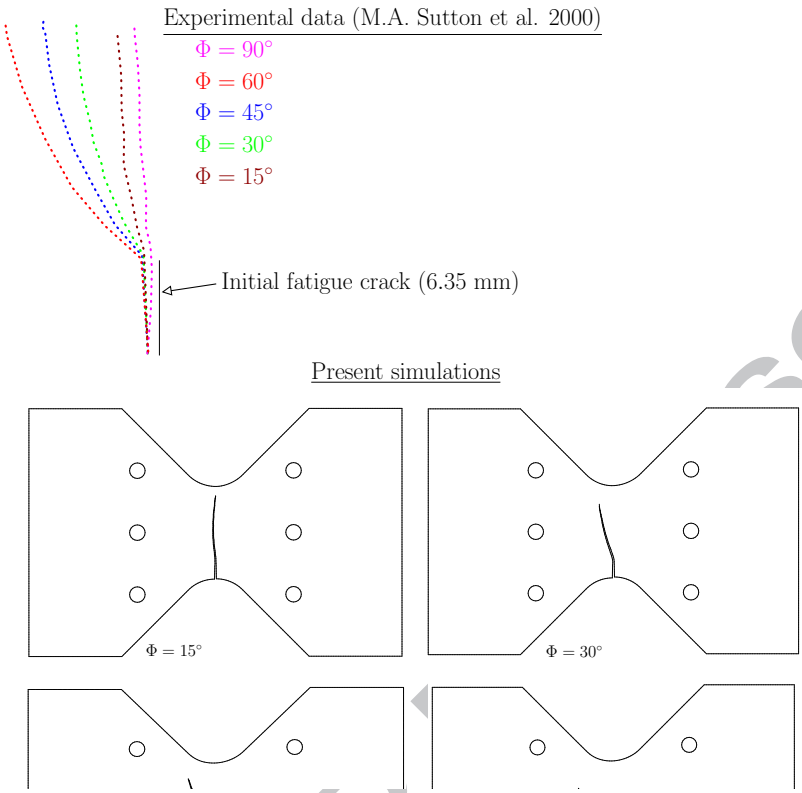

Figure 26: ARCAN test: crack path compared with the experimental results of Sutton *et al. [60]*. Also shown is the void fraction contour plot.

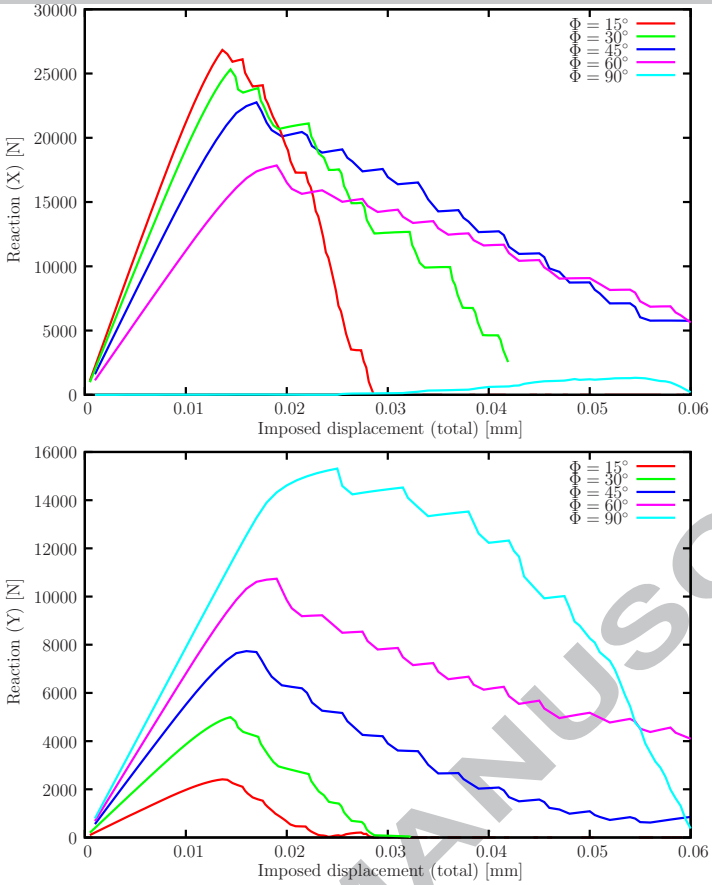

Figure 27: ARCAN test: Reactions components resulting from imposed displacement.

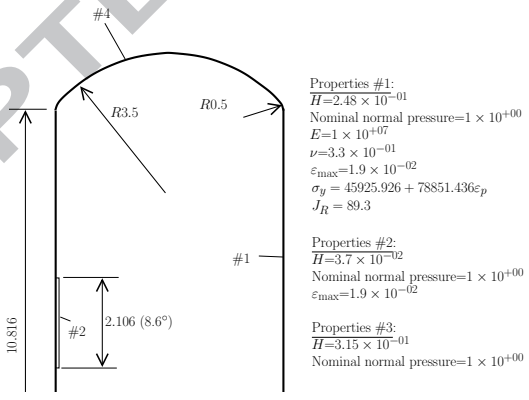

Figure 28: Pressure vessel with slot, corresponding to specimen #12 of Kitching and Zarrabi (cf. [39]).

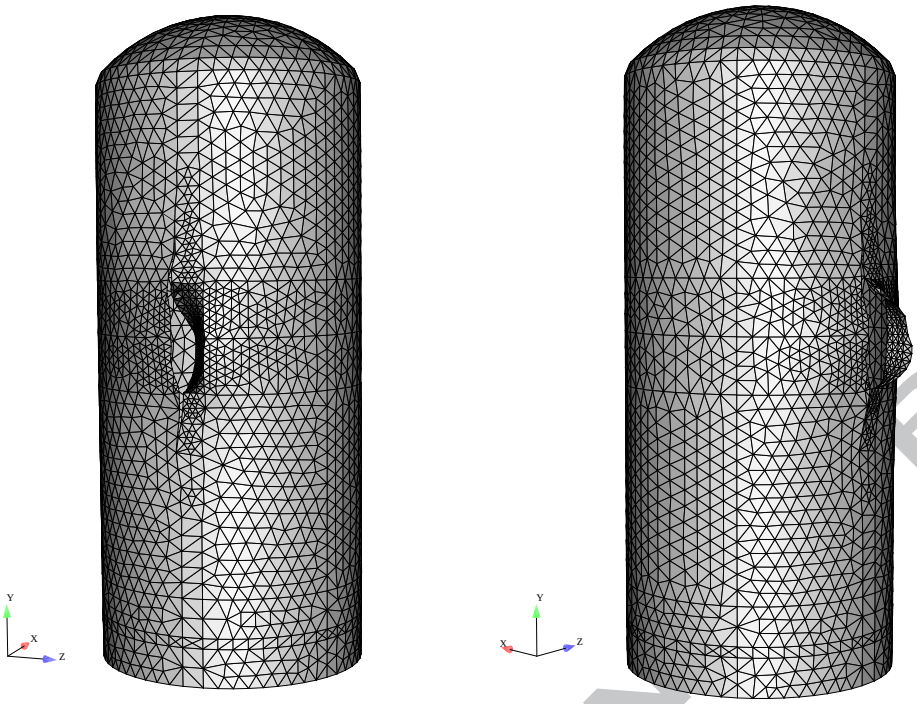

Figure 29: Cracked pressure vessel.

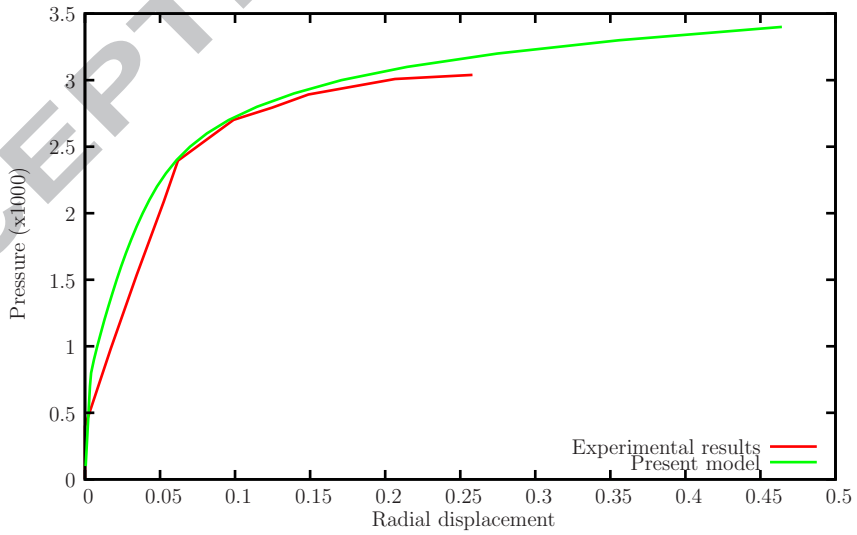

Figure 30: Pressure vessel with slot: comparison with experimental results (cf. [39]).

5 Conclusions

The simple algorithm of edge rotation for computational fracture provides an advantageous alternative to the tip remeshing algorithm proposed by the Authors (cf. [9, 16, 11, 10, 14]). Crack paths are more regular, Newton-Raphson convergence is better and less mesh distortion occurs. We found that both for brittle, quasi-brittle and ductile fracture, classical benchmarks perform at least as well as alternative techniques. We note that, although quadrilaterals can be used, some elements can suffer a too severe distortion and negative Jacobians. Recent enrichment techniques also show remarkable accuracy, but are more limiting for large amplitude displacements and the application to elasto-plastic problems is not clear. A subsequent manuscript is in preparation, applying the present algorithm to full 3D computational fracture.

Acknowledgments

The authors gratefully acknowledge financing from the "Fundação para a Ciência e a Tecnologia" under the Project PTDC/EME-PME/108751 and the Program COMPETE FCOMP-01-0124-FEDER-010267.

References

[1] J. Alfaiate, A. Simone, and L.J. Sluys. A new approach to strong embedded discontinuities. In N. Bicanic, R. de Borst, H. Mang, and G. Meschke, editors, *Computational Modelling of Concrete Structures, EURO-C 2003*, St. Johann im Pongau, Salzburger Land, Austria, March 2003.

[2] J. Alfaiate, G.N. Wells, and L.J. Sluys. On the use of embedded discontinuity elements with crack path continuity for mode-I and mixed-mode fracture. *Eng Fract Mech*, 69:661–686, 2002.

[3] G. Allaire, F. Jouve, and Van Goethem. Damage and fracture evolution in brittle materials by shape optimization methods. *J Comput Phys*, 230(12):5010–5044, 2011.

[4] S.S. Antman. *Nonlinear problems of elasticity*. Springer, Second edition, 2005.

[5] P. Areias and T. Belytschko. Analysis of three-dimensional crack initiation and propagation using the extended finite element method. *Int J Numer Meth Eng*, 63:760–788, 2005.

[6] P. Areias and T. Belytschko. Non-linear analysis of shells with arbitrary evolving cracks using xfem. *Int J Numer Meth Eng*, 62:384–415, 2005.

[7] P. Areias and T. Belytschko. Analysis of finite strain anisotropic elastoplastic fracture in thin plates and shells. *J Aerospace Eng*, 19(4):259–270, 2006.

[8] P. Areias, J.M.A. César de Sá, C.A. Conceição António, J.A.S.A.O. Carneiro, and V.M.P. Teixeira. Strong displacement discontinuities and Lagrange multipliers in the analysis of finite displacement fracture problems. *Comput Mech*, 35:54–71, 2004.

[9] P. Areias, D. Dias-da-Costa, J. Alfaiate, and E. Júlio. Arbitrary bi-dimensional finite strain cohesive crack propagation. *Comput Mech*, 45(1):61–75, 2009.

[10] P. Areias, D. Dias-da Costa, E.B. Pires, and J. Infante Barbosa. A new semi-implicit formulation for multiple-surface flow rules in multiplicative plasticity. *Comput Mech*, 49:545–564, 2012.

[11] P. Areias, J. Garção, E.B. Pires, and J. Infante Barbosa. Exact corotational shell for finite strains and fracture. *Comput Mech*, 48:385–406, 2011.

[12] P. Areias and T. Rabczuk. Quasi-static crack propagation in plane and plate structures using set-valued traction-separation laws. *Int J Numer Meth Eng*, 2007.

[13] P. Areias, M. Ritto-Corrêa, and J.A.C. Martins. Finite strain plasticity, the stress condition and a complete shell model. *Comput Mech*, 45:189–209, 2010.

[14] P. Areias, H.G. Silva, N. Van Goethem, and M. Bezzeghoud. Damage-based fracture with electro-magnetic coupling. *Comput Mech*, 2012. In Press.

[15] P. Areias, J.H. Song, and T. Belytschko. Analysis of fracture in thin shells by overlapping paired elements. *Comp Method Appl M*, 195(41-43):5343–5360, 2006.

[16] P. Areias, N. Van Goethem, and E.B. Pires. A damage model for ductile crack initiation and propagation. *Comput Mech*, 47(6):641–656, 2011.

[17] D.N. Arnold, F. Brezzi, and M. Fortin. A stable finite element for the Stokes equations. *Calcolo*, XXI(IV):337–344, 1984.

[18] F. Barpi and S. Valente. Numerical simulation of prenotched gravity dam models. *J Eng Mech-ASCE*, 126(6):611–619, 2000.

[19] Z.P. Bažant and J. Planas. *Fracture and size effect in concrete and other quasibrittle materials*. CRC Press, 1998.

[20] T. Belytschko and T. Black. Elastic crack growth in finite elements with minimal remeshing. *Int J Numer Meth Eng*, 45:601–620, 1999.

[21] T.N. Bittencourt, Ingraffea A.R. Wawrzynek, P.A., and J.L. Sousa. Quasi-automatic simulation of crack propagation for 2D LEFM problems. *Eng Fract Mech*, 55(2):321–334, 1996.

[22] P. Bocca, A. Carpinteri, and S. Valente. Mixed mode fracture of concrete. *Int J Solids Struct*, 27(9):1139–1153, 1991.

[23] S. Bordas, S. Natarajan, S. Dal Pont, T. Rabczuk, P. Kerfriden, D.R. Mahapatra, D. Noel, and Z. Gao. On the performance of strain smoothing for enriched finite element approximations (xfem/gfem/pufem). *International Journal for Numerical Methods in Engineering*, 86:637–666, 2011.

[24] S. Bordas, T. Rabczuk, H. Nguyen-Xuan, S. Natarajan, T. Bog, V.P. Nguyen, Q. Do Minh, and H. Nguyen Vinh. Strain smoothing in fem and xfem. *Computers & Structures*, 88:1419–1443, 2010.

[25] B. Bourdin, G.A. Francfort, and J.-J. Marigo. Numerical experiments in revisited brittle fracture. *J Mech Phys Solids*, 48:797–826, 2000.

[26] K.B. Broberg. *Cracks and Fracture*. Academic Press, 1999.

[27] Y. Cai, X.Y. Zhuang, and H. Zhu. A generalized and efficient method for finite cover generation in the numerical manifold method.

[28] A. Carpinteri. Post-peak and post-bifurcation analysis of cohesive crack propagation. *Eng Fract Mech*, 32:265–278, 1989.

[29] E.W.V. Chaves. PhD thesis, Universitat Politècnica de Catalunya, Escola Tècnica Superior D'Enginyers de Camins, Canals I Ports, Barcelona, Spain, February 2003.

[30] D. Colombo and M. Giglio. A methodology for automatic crack propagation modelling in planar and shell fe models. *Eng Fract Mech*, 73:490–504, 2006.

[31] Alfaiate J. Sluys L.J. Areias P. Júlio E. Dias-da Costa, D. An embedded formulation with conforming finite elements to capture strong discontinuities. *Int J Numer Meth Eng*, 93(2):224–244, 2013.

[32] D. Dias-da-Costa, J. Alfaiate, L.J. Sluys, and E. Júlio. A discrete strong discontinuity approach. *Eng Fract Mech*, 76(9):1176–1201, 2009.

[33] M. Elices, G.V. Guinea, J. Gómez, and J. Planas. The cohesive zone model: advantages, limitations and challenges. *Eng Fract Mech*, 69:137–163, 2002.

[34] F. Erdogan and G.C. Sih. On the crack extension in plates under plane loading and transverse shear. *J Bas Eng*, 85:519–527, 1963.

[35] G. Etse and K. Willam. Failure analysis of elastoviscoplastic material models. *J Eng Mech-ASCE*, 125:60–69, 1999.

[36] C. Glocker. *Set-valued force laws, dynamics of non-smooth systems*, volume 1 of *Lecture notes in applied mechanics*. Springer-Verlag, Berlin, 2001.

[37] A. Hansbo and P. Hansbo. A finite element method for the simulation of strong and weak discontinuities in solid mechanics. *Comp Method Appl M*, 193:3523–3540, 2004.

[38] B.L. Karihaloo and Q.Z. Xiao. Modelling of stationary and growing cracks in FE framework without remeshing: a state-of-the-art review. *Comput Struct*, 81:119–129, 2003.

[39] R. Kitching and K. Zarrabi. Limit and burst pressures for cylindrical shells with part-through slots. *Int J Pres Ves Pip*, 10:235–270, 1982.

[40] R. Krueger. The virtual crack closure technique: History, approach and applications. ICASE CR-2002-211628, NASA, 2002.

[41] G. Legrain, N. Moës, and E. Verron. Stress analysis around crack tips in finite strain problems using the extended finite element method. *Int J Numer Meth Eng*, 63:290–314, 2005.

[42] S. Loehnert and T. Belytschko. A multiscale projection method for macro/microcrack simulations. *Int J Numer Meth Eng*, 71:1466–1482, 2007.

[43] F. Ma, X. Deng, M.A. Sutton, and Jr. Newman, J.C. *Mixed-mode crack behavior*, chapter A CTOD-based mixed-mode fracture criterion, pages 86–110. Number STP 1359. ASTM American Society for Testing and Materials, West Conshohocken, PA, 1999.

[44] C. Miehe and E. Gürses. A robust algorithm for configurational-force-driven brittle crack propagation with $r-$adaptive mesh alignment. *Int J Numer Meth Eng*, 72:127–155, 2007.

[45] N. Moës and T. Belytschko. Extended finite element method for cohesive crack growth. *Eng Fract Mech*, 69:813–833, 2002.

[46] N. Moës, J. Dolbow, and T. Belytschko. A finite element method for crack growth without remeshing. *Int J Numer Meth Eng*, 46:131–150, 1999.

[47] N. Moës, J. Dolbow, and T. Belytschko. A finite element method for crack growth without remeshing. *Int J Numer Meth Eng*, 46:131–150, 1999.

[48] J. Oliver. A consistent characteristic length for smeared cracking models. *Int J Numer Meth Eng*, 28:461–474, 1989.

[49] J. Oliver. Continuum modelling of strong discontinuities in solid mechanics using damage models. *Comput Mech*, 17:49–61, 1995.

[50] J. Planas, M. Elices, G.V. Guinea, D.A. Gómez, Cendón, and I. Arbilla. Generalizations and specializations of cohesive crack models. *Eng Fract Mech*, 70:1759–1776, 1996.

[51] T. Rabczuk, J. Akkermann, and J. Eibl. A numerical model for reinforced concrete structures. *International Journal of Solids and Structures*, 42(5-6):1327–1354, 2005.

[52] T. Rabczuk and P. Areias. A meshfree thin shell for arbitrary evolving cracks based on an external enrichment. *Comput Model Eng Sci*, 16(2):115–130, 2006.

[53] T. Rabczuk, P. Areias, and T. Belytschko. A meshfree thin shell method for non-linear dynamic fracture. *Int J Numer Meth Eng*, 72:524–548, 2007.

[54] T. Rabczuk and T. Belytschko. Cracking particles: a simplified meshfree method for arbitrary evolving cracks. *Int J Numer Meth Eng*, 61:2316–2343, 2004.

[55] T. Rabczuk, T. Belytschko, and S.P. Xiao. Stable particle methods based on lagrangian kernels. *Computer Methods in Applied Mechanics and Engineering*, 193:1035–1063, 2004.

[56] T. Rabczuk and J. Eibl. Simulation of high velocity concrete fragmentation using sph/mlsph. *International Journal for Numerical Methods in Engineering*, 56:1421–1444, 2003.

[57] E.F. Rybicki and M.F. Kanninen. A finite element calculation of stress intensity factors by a modified crack closure integral. *Eng Fract Mech*, 9(4):931–938, 1977.

[58] E. Schlangen. *Experimental and numerical analysis of fracture processes in concrete*. PhD thesis, Delft, 1993.

[59] H.L. Schreyer and Z. Chen. One-dimensional softening with localization. *J Appl Mech-ASME*, 53:791–797, 1986.

[60] M.A. Sutton, X. Deng, F. Ma, J.C. Newman Jr., and M. James. Development and application of a crack tip opening displacement-based mixed mode fracture criterion. *Int J Solids Struct*, 37:3591–3618, 2000.

[61] X. Teng and T. Wierzbicki. Evaluation of six fracture models in high velocity perforation. *Eng Fract Mech*, 73:1653–1678, 2006.

[62] N. Van Goethem and P. Areias. A damage-based temperature-dependent model for ductile fracture with finite strains and configurational forces. *Int J Fracture*, 178:215–232, 2012.

[63] N. Vu Bac, H. Nguyen-Xuan, L. Chenand S. Bordas, P. Kerfriden, R.N. Simpson, G.R. Liu, and T. Rabczuk. A node-based smoothed extended finite element method (nsxfem) for fracture analysis. *CMES-Computer Modeling in Engineering & Sciences*, 1898:1–25, 2011.

[64] X.Y. Zhuang, C. Augarde, and K. Mathisen. Fracture modelling using meshless methods and level sets in 3d: framework and modelling. *Int J Numer Meth Eng*, 92:969–998, 2012.

[65] X.Y. Zhuang, C. Heaney, and C. Augarde. On error control in the element-free galerkin method.